RevMexAA (Serie de Conferencias), **7**, 143–148 (1998)

FREE-FREE RADIATION FROM DENSE INTERSTELLAR SHOCK WAVES

P. Ghavamian and P. Hartigan

Department of Space Physics & Astronomy, Rice University, Houston, TX 77005-1892;
parviz@rice.edu

RESUMEN

Se presentan cálculos detallados de la emisión libre-libre de choque, en donde el gas puede ser ópticamente denso en frecuencias de radio. Resolvemos la ecuación de transporte radiativo en las frecuencias 1.5, 5 y 15 GHz para una familia de modelos planos de choques, los cuales cubren amplios intervalos de densidades ($1000 \leq n_0 \leq 10^9$ cm^{-3}, de velocidades de choque ($30 \leq V_0 \leq 300$ km s^{-1}) y de ángulos visuales ($0° \leq \Theta \leq 85°$). Aplicamos nuestros modelos a los datos observacionales y predecimos los parámetros del choque para HH 1-2 (ópticamente delgados) y varias fuentes de radio en Cep A (parcialmente opacas). En el caso de HH 1-2, se encuentra una concordancia entre los parámetros de choque que derivamos y aquellos pronosticados por las líneas de Hα y [S II]. Nuestros modelos para Cep A indican grandes ángulos visuales ($\sim 70°$), altas densidades ($\geq 10^4$ cm^{-3}) y altas velocidades de choque (~ 250 km s^{-1}).

ABSTRACT

We present detailed calculations of the free-free emission from shocks where the gas may be optically thick at radio frequencies. We solve the radiative transfer equation at frequencies of 1.5, 5 and 15 GHz for a family of planar shock models which cover a wide range of densities ($1000 \leq n_0 \leq 10^9$ cm^{-3}) shock velocities ($30 \leq V_0 \leq 300$ km s^{-1}), and viewing angles ($0° \leq \Theta \leq 85°$). We apply our models to observational data and predict shock parameters for HH 1-2 (optically thin) and several radio sources in Cep A East (partially opaque). In the case of HH 1-2, we find very good agreement between our derived shock parameters and those predicted by the Hα and [S II] lines. Our models for Cep A indicate large viewing angles ($\sim 70°$), high densities ($\geq 10^4$ cm^{-3}) and high shock velocities (~ 250 km s^{-1}).

Key words: **ISM: JETS AND OUTFLOWS — RADIATIVE TRANSFER — RADIO CONTINUUM: ISM — SHOCK WAVES**

1. INTRODUCTION

Through numerous multiwavelength studies, a picture has emerged of HH objects as radiative shock waves produced by mass ejections from young stellar objects (YSOs), followed by dense, low excitation jets which do not always produce detectable emission. So far, attempts to trace the mass ejections close to their sources have been limited to long wavelength observations (IR and radio)due to extremely high extinction from the surrounding cloud. The detection of radio continuum by Pravdo et al. (1985) in HH 1 and 2 offered a new method for tracing the postshock ionized gas in these flows, and further study of this region (Rodríguez et al. 1990) and others such as HH 80-81 (Rodríguez et al. 1989; Martí, Rodríguez, & Reipurth 1993), HH 32 (Anglada et al. 1992) and HH 12 (Snell & Bally 1986) has proved to be quite valuable in probing outflows back to their points of origin. So far, limitations in instrumental sensitivity have produced a selection effect where only the faster, denser shocks are detected (≥ 100 km s^{-1}, n$\sim 10^3$–10^5 cm^{-3}, Curiel 1995). At these shock velocities and densities, the postshock gas will be partially opaque at GigaHertz frequencies, especially at steep viewing angles. It is, therefore, important to solve the free-free radiative transfer equation when modelling the emission from deeply embedded radio sources. We have included this calculation in our shock models, which utilize the Cox-Raymond numerical shock code (1985).

2. THE NUMERICAL CALCULATION

Our shock structures are generated by Cox-Raymond equilibrium preionization models (1985) and preshock ionization fractions of Shull & McKee (1979). After solving the Rankine-Hugoniot jump conditions, the code

computes the enthalpy radiated away by a parcel of gas in a series of time steps, and determines its corresponding temperature, density and ionization fraction. We assume a preshock magnetic field of 1 μG, low enough to neglect the influence of magnetic pressure on the free-free emission. After M steps, the gas has cooled to 1000 K, and the accumulated optical depth $\tau_\nu(M)$ is given by

$$\tau_\nu(M) = \sum_{n=1}^{M} \frac{j_\nu(n)\Delta s_n}{B_\nu(T_n)}, \tag{1}$$

where Δs_n is the distance travelled by the parcel of gas between steps $n-1$ and n, and the source function $B_\nu(T) = 2\nu^2 kT/c^2$. At the nth step, the volume emissivity $j_\nu(T_n)$ (ergs s^{-1} cm^{-3} Hz^{-1} str^{-1}) is given by

$$j_\nu(n) \approx 5.44 \times 10^{-39} Z^2 N_e(n) N_i(n) \frac{g_n(\nu, T_n)}{T_n^{1/2}}, \tag{2}$$

where N_e and N_i denote the electron and ion number densities, and $g_n(\nu, T_n)$ is the velocity-averaged Gaunt factor (Rybicki & Lightman 1979). For an external observer at viewing angle Θ, the free-free intensity is

$$I_\nu(\Theta) = \sum_{n=1}^{M} j_\nu(n) e^{-\tau_\nu(n) sec\,\Theta} \Delta s_n sec\,\Theta. \tag{3}$$

3. RESULTS

3.1. Structural Characteristics of the Shock Models

Between 80 and 110 km s^{-1}, the rapid rise in preshock ionization fraction divides the shock models into three groups: those that encounter fully neutral gas, those that encounter partially ionized gas, and those that pass through completely ionized gas. To demonstrate the differences in cooling behavior between the three groups, we focus our attention on three models: 50 km s^{-1} ($\leq$ 1% H preionization), 90 km s^{-1} (38% H preionization) and 140 km s^{-1} (100% H preionization). These models are labelled E50, E90 and E140.

The influence of postshock gas on the free-free radiative transfer can be illustrated by a log τ_ν-log T diagram. Figure 1 shows that for fixed shock velocity, one feature which distinguishes the low density models from high density ones is the shape of the log τ_ν-log T curves in the recombination zone, where the higher recombination rate at high density results in a sharper temperature decline below 10^4 K. Increasing the preshock density translates the curves toward the right, leaving a larger portion of each curve in the region labelled "optically thick". The immediate postshock temperature in E90 drops most rapidly because in this case a sizeable portion of the flow kinetic energy is channelled into collisional ionization. On the other hand, the temperature declines slowly in models E50 and E140 because in the former case there is not enough energy to ionize the gas, while in the latter case the gas is almost completely ionized and cannot cool efficiently by forbidden line emission above 10^5 K.

As Fig. 1 shows, the accumulated free-free optical depth scales linearly with preshock density. This results from the dependence of $\tau_\nu(M)$ on $n_0^2 d_c$ (eq. 1), where d_c is the cooling length of the gas, defined as the distance a shocked parcel of gas must travel downstream to reach 10^4 K. According to Hartigan, Raymond, & Hartmann (1987), $d_c \sim \frac{1}{n_0}$, where n_0 is the preshock number density (assuming negligible magnetic pressure support near 10^4K), hence $\tau_\nu(M) \sim n_0$.

3.2. Spectral Indices

The influence of preshock density and viewing angle Θ on the shape of the free-free spectrum is shown in in Fig. 2, where spectral index curves are shown between 1.5 and 15 GHz for models E50, E90, E140 and E250. We define the spectral index via

$$\alpha_{\nu_1\nu_2}(\Theta) \equiv \frac{log(I_{\nu_1}(\Theta)/I_{\nu_2}(\Theta))}{log(\nu_1/\nu_2)}, \tag{4}$$

where $I_\nu(\Theta)$ is the free-free intensity and $\nu_1 < \nu_2$. At shock velocities above 100 km s^{-1}, the spectral index does not increase monotonically with preshock density as one would expect for a single temperature plasma, but bends downward before finally approaching 2. As the preshock density is increased at each shock velocity, there

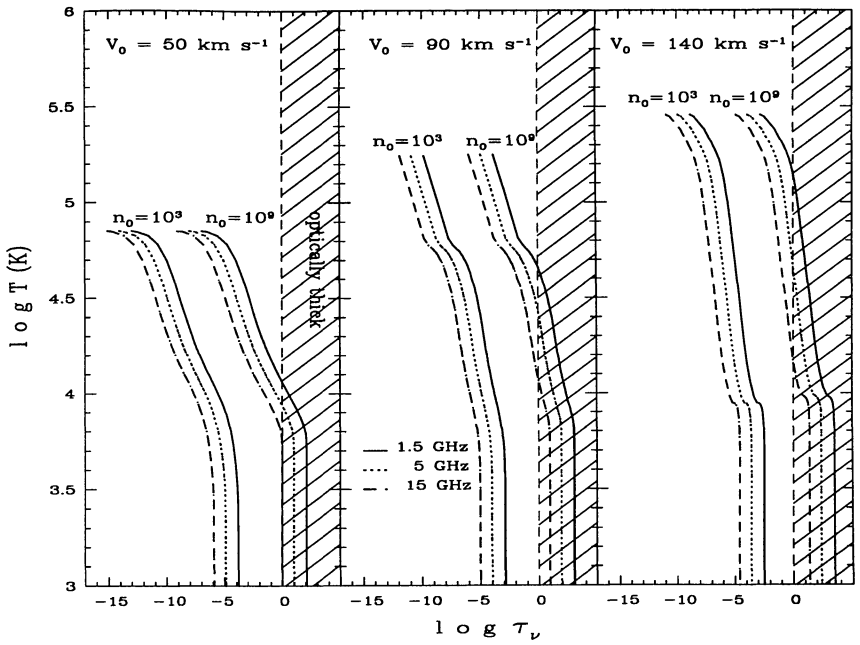

Fig. 1. Accumulated free-free optical depth vs. temperature in the postshock region for models E50 (no precursor), E90 (partial preionization) and E140 (full preionization). The curves are traced by a cooling parcel of gas at constant frequency. The shaded region is opaque to an external observer viewing the shock face-on.

will be three transition densities where first 1.5 GHz, then 5 GHz and finally 15 GHz become optically thick. At high shock velocities, spectral index bending occurs during this transition, and is caused by the structure of the recombination zone near 10^4 K, where the postshock gas slows down rapidly and piles up into a dense shell.

Figure 2 indicates that the spectral index bend moves toward lower preshock densities when Θ is large. When $\tau_\nu \ll 1$, the free-free intensity increases as $T_b \, sec\,\Theta$, where T_b is the brightness temperature of the gas (eq. 3). If $\tau_\nu \gtrsim 1$, the exponential term in eq. 3 dominates and the emission begins to drop as Θ is increased. Our full grid results will appear elsewhere (Ghavamian & Hartigan 1997).

4. APPLICATIONS

4.1. HH 1 and 2

The HH 1-2 system was studied at high angular resolution with the VLA by Rodríguez et al. (1990) at 1.5, 5 and 15 GHz. They reported flat spectral indices for both HH objects (~ -0.1), consistent with optically thin free-free emission. In this case, we linearly interpolated our model fluxes at n_0=1000 cm^{-3} to their observed values. Rodríguez et al. reported that the radio condensations match the optical knots HH 1F and HH 2A′ to within 1″. The bow shock models of Hartigan et al. (1987) suggest a viewing angle Θ of $\sim 70°$ for HH 1F and $\sim 80°$ for HH 2A′, with preshock densities $\geq$ 500 cm^{-3}. The line widths indicate shock velocities between 100 and 250 km s^{-1}. We used the reported angular sizes of Rodríguez et al. (1990) to find the free-free intensities at 1.5, 5 and 15 GHz, then linearly interpolated our model fluxes at n_0 = 1000 cm^{-3} to the observed values. Table 1 shows that our predicted radio fluxes tend to be higher than those observed; this is due to our models' planar shock geometry. In reality, the bow shock apex travels faster than the wings, hence the effective surface area moving $\geq$ 100 km s^{-1} covers a smaller portion of the shock front, and the predicted free-free flux will be lowered. However, even without incorporating the bow shock geometry, the agreement between calculated shock parameters and the HRH values is quite good. Before the bow shock models of Hartigan et al. (1987) became available, Curiel, Cantó, & Rodríguez (1987) made a radiative transfer calculation to model the radio emission from HH 1 and 2. They used the old radio data of Pravdo et al. (1985), therefore, there are differences between their shock derived shock parameters and ours.

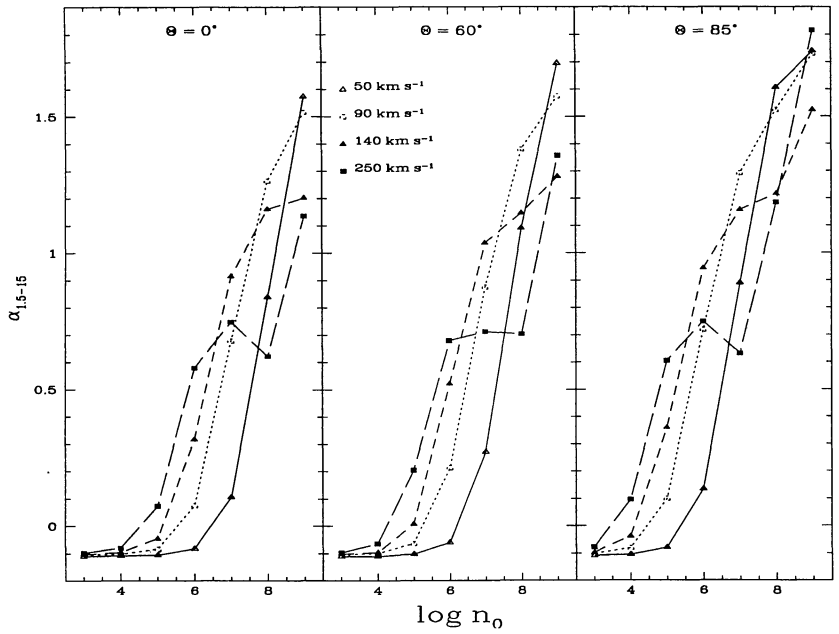

Fig. 2. Spectral index vs. preshock density between 1.5 and 15 GHz, for models E50, E90, E140 and E250. Indices close to −0.1 indicate optically thin emission, and indices close to 2 indicate optically thick emission. $\alpha_{\nu_1\nu_2}$ becomes more positive at larger viewing angles Θ because the observer's line of sight intersects more gas.

4.2. Cep A East

The Cep A region was first identified by Sargent (1977) as an active site of star formation, and subsequent radio observations by Hughes & Wouterloot (1982) resolved its ionized components into two parts, Cep A East and Cep A West. Hughes & Wouterloot identified 14 compact components in the radio continuum, aligned in a stringlike fashion. Joyce & Simon (1986) suggested that a shocked stellar jet from a nearby YSO is responsible for the radio emission, an assertion supported by Garay et al. (1996).

To test the shocked wind scenario, we have used VLA data of Cepheus A East from Garay et al. (1996) to predict shock parameters from our plane parallel models. We used the reported angular sizes and flux densities at 1.5, 5 and 15 GHz to determine intensities and spectral indices of thermal sources 3b, 3c, and 7a. We did not attempt to model sources with nonthermal spectral indices (< -0.1) because our numerical code does not compute nonthermal emission. The angular resolution of the VLA measurements was $\approx 1''$ at all three frequencies; therefore, the sources are either barely resolved or uresolved and we have only an upper limit on the angular sizes. Our derived intensities depend on the angular sizes, and this adds uncertainty into our comparisons with model predictions. Our usage of a planar shock geometry introduces another source of uncertainty, since the real shocks are likely to follow a curved shape. Nevertheless, as Table 1 shows, we were able to reproduce the observed fluxes reasonably well, although as expected, the agreement does not hold equally well at all frequencies.

Our analysis supports Garay et al.'s conclusion that the thermal string sources in Cep A are shock excited. In addition, our results suggest shock velocities ≥ 100 km s^{-1}, typical of HH objects, and steep viewing angles $\geq 60°$. Since the sources exhibit very small proper motions ($\sim 0.02''$ yr^{-1}), our viewing angle estimates suggest that sources 3b,c and 7a represent the shock heated gas of a stellar wind impinging on dense, quasistationary cloudlets. Garay et al. found that the string 7 sources mark the edge of the dense NH_3 condensation Cep A-3 mapped by Torelles et al. (1993).

5. SUMMARY

We have devised a grid of planar shock models which predict the free-free radio emission for arbitrarily high optical depths, and have estimated the influence of the preshock density, shock velocity and viewing angle

TABLE 1

PLANAR SHOCK PARAMETERS FOR OBSERVED RADIO SOURCES

	Observed Flux (mJy)			Planar Model Flux (mJy)			Planar Model Parameters		
Object[a,b]	1.5 GHz	5 GHz	15 GHz	1.5 GHz	5 GHz	15 GHz	n_0	V_0 (km s^{-1})	Θ
HH 1	0.92	0.46	0.78	0.92	0.83	0.73	1000	100	80°
HH 2	0.94	1.3	0.98	1.02	0.91	0.81	500	160	60°
Cep A 3b	4.2±0.1	5.0±0.1	4.1±0.2	5.4	5.9	5.6	10^5	140	0°
Cep A 3c	2.1±0.1	3.7±0.1	5.2±0.2	2.7	5.6	5.5	10^4	250	70°
Cep A 7a	9.5±0.2	9.6±0.1	6.9±0.3	13.6	9.4	7.1	10^4	300	75°

[a]HH 1-2 data from Rodríguez et al. (1990)

[b]Cep A data from VLA observations of Garay et al. (1996)

on the spectral indices. This is the first attempt to generate systematic, quantitative predictions for comparison with observational data. Our primary results are:

1. At each shock velocity, the free-free optical depth τ_ν scales linearly with preshock density, while the intensity does so only when τ_ν is small near 10^4 K. For face-on shocks slower than 200 km s^{-1}, emission at 1.5 GHz becomes optically thick at a preshock density of 10^6 cm^{-3}, while emission at 15 GHz becomes optically thick at 10^9 cm^{-3}. At 1.5 GHz, the transition to the optically thick regime begins at 10^5 cm^{-3} for shocks faster than 200 km s^{-1}.

2. Above 100 km s^{-1}, the spectral index does not monotonically approach 2 with increasing preshock density as one would expect for a single temperature plasma, but bends downward for a small subrange of preshock densities. This feature occurs whenever $\tau_{\nu 1} > 1$ and $\tau_{\nu 2} \approx 1$ ($\nu_1 < \nu_2$) near 10^4K, and is caused by the high free-free volume emissivity near 10^4 K.

5. Our planar models can match the free-free fluxes and spectral indices of both optically visible shocks, such as HH 1 and 2, and heavily obscured ones, such as the thermal sources (suspected shocked cloudlets) in the Cep A East region.

This work was supported by grant D70832 from Rice University.

Note: After this paper was written, it came to our attention that for shock velocities exceeding 120 km s^{-1}, the fully ionized precursor can itself exhibit a substantial optical depth to free-free radiation emerging from the postshock zone. This result will change the preshock parameters quoted in Table 1 for the Cep A sources; our revised calculations and results will appear in Chavamian & Hartigan (1997).

REFERENCES

Anglada, G., Rodríguez, L. F., Cantó, J., Estalella, R., & Torelles, J. M. 1992, ApJ, 395, 494
Cox, D., & Raymond, J. 1985, ApJ, 298, 651
Curiel, S. 1995, in Circumstellar Disks, Outflows and Star Formation, ed. S. Lizano & J. M. Torrelles, RevMexAASC, 1, 59
Curiel, S., Cantó, J., & Rodríguez, L. F. 1987, RevMexAA, 14, 595.
Garay, G., Ramírez, S., Rodríguez, L. F., Curiel, S. & Torelles, J. M. 1996, ApJ, 459, 193
Ghavamian, P. & Hartigan, P. 1997, ApJ, in press
Hartigan, P., Raymond, J., & Hartmann, L. 1987, ApJ, 316, 323
Hughes, V. A., & Wouterloot, J. G. A. 1982, A&A, 106, 171
Joyce, R. R., & Simon, T. 1986, AJ, 91, 113
Martí, J., Rodríguez, L. F., & Reipurth, B. 1993, ApJ, 416, 208
Pravdo, S. H., Rodríguez, L. F., Curiel, S., Cantó, J., Torelles, J. M., Becker, R. H., & Sellgren, K. 1985, ApJ, 293, L35
Rodríguez, L. F., Ho, P. T. P., Torelles, J. M., Curiel, S., & Cantó, J. 1990, ApJ, 352, 645

Rodríguez, L. F., Curiel, S., Moran, J. M., Mirabel, I. F., Roth, M., & Garay, G. 1989, ApJ, 346, L85
Rybicki, G. B., & Lightman, A. P. 1979, Radiative Processes in Astrophysics, (New York: Wiley & Sons)
Sargent, A. I. 1977, ApJ, 218, 736
Shull, J. M., & McKee, C. F., 1979, ApJ, 227, 131
Snell, R. L., & Bally, J. 1986, ApJ, 303, 683
Torelles, J. M., Verdes-Montenegro, L., Ho, P. T. P., Rodríguez, L. F., & Cantó, J. 1993, ApJ, 410, 202

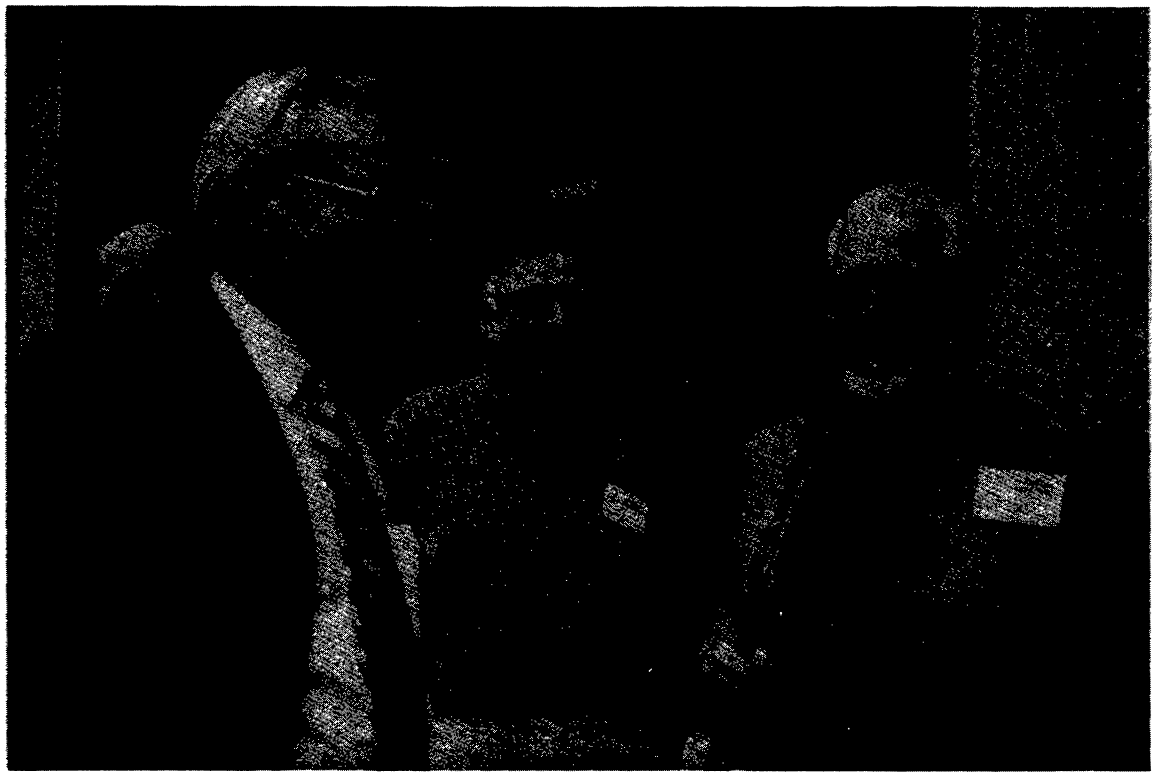

Manuel Peimbert, Gene Capriotti, and Don Cox.